PCCP

ROYAL SOCIETY OF CHEMISTRY

PAPER

Published on 02 July 2026

Cite this: *Phys. Chem. Chem. Phys.*, 2026, **28**, 17942

How ice grows on calcite

Florian Schneider, *[a] Lea Klausfering,[a] Isaac Azahel Ruiz Alvarado,[b] Thomas Koop,[c] Ralf Bechstein,[a] Wolf Gero Schmidt[b] and Angelika Kühnle[a]

Received 26th May 2026,
Accepted 30th June 2026

DOI: 10.1039/d6cp01936f

rsc.li/pccp

Ice nucleation is ubiquitous in nature and technology and decisive for a wide range of fields, including biology, geochemistry and environmental science. In most cases, ice nucleation occurs heterogeneously due to the presence of an ice nucleating material. Despite its importance, we still largely fail to reliably predict the ice nucleation efficacy of a given material. A particularly puzzling example is calcite, a major constituent of rocks in the Earth's crust. Although calcite possesses a high hydrophilicity, it is basically inactive in ice nucleation. Here, we combine non-contact atomic force microscopy with temperature programmed desorption measurements to investigate water multilayer formation and ice growth on calcite's (10.4) surface in ultrahigh vacuum. Adsorption of water results in the formation of up to four water layers. Interestingly, the fourth layer is observed to be metastable, as it shrinks as soon as crystalline ice nucleates. The molecular structure of the water layers is governed by the underlying calcite lattice, highlighting the strong impact of the surface. This strong templating effect of the substrate prevents the water from adopting an ice-like structure even in the fourth layer. Our results, thus, provide an explanation for the poor ice-nucleating efficacy of calcite and underscore that ice nucleation efficacy cannot be predicted based on a single descriptor.

1. Introduction

Nucleation plays a decisive role in a multitude of natural as well as technological processes. Prominent examples include biomineralization[1] or the crystallization of active substances in pharmacy.[2] A very common and exceedingly important nucleation process is the freezing of water. Due to the high kinetic barrier of homogeneous ice nucleation, pure water can be cooled down to about 236 K without freezing.[3,4] A vast variety of particles ranging from biological material[5] to mineral dusts[6,7] are known to reduce this kinetic barrier by inducing heterogeneous nucleation. The ice nucleation efficacy of several types of particles has been quantified with droplet freezing experiments.[6–9] Moreover, the effect of surface morphology has been investigated with optical microscopy[10–12] and scanning electron microscopy,[13] revealing the importance of steps and pores in enhancing ice nucleation on the micrometer scale.[14]

These mesoscopic experiments have been expanded by studies that systematically tune the nanoscale surface morphology using a wide range of materials,[15] including adsorbed gold nanodots,[16] metal–organic frameworks,[17] and DNA origami.[18] Collectively, these studies indicate that increasing nanoscale roughness results in a lower ice nucleating efficacy. Further, nanoscopic investigations of water coverages ranging from single molecules up to bulk ice on (noble) metal surfaces have been performed under ultrahigh vacuum conditions.[19–21] Depending on the specific metal, the binding energy of water on metal surfaces has been calculated to span the range from 0.1 eV to 0.4 eV.[22] Thus, the strength of the water–metal interaction is comparable to that of the hydrogen bond between two water molecules, which ranges between 0.1 eV and 0.3 eV.[23] Optimizing the subtle balance between these two interactions allows the formation of a broad variety of adsorption structures.[20]

However, despite these efforts, our ability to predict the ice nucleation efficacy of a given material is still rather limited.[24,25]

The influence of surface parameters such as symmetry, lattice constant and binding energy on the ice nucleation efficacy of a given surface has been systematically investigated with theoretical simulations.[26–28] These investigations have shown that no single descriptor is sufficient to predict the ice nucleation efficacy.[26] Instead, a combination of these parameters is necessary due to their complex interplay. For immersion freezing Davies *et al.* proposed that the interfacial structure of water, as a single descriptor, is sufficient to predict ice nucleation.[25] However, the interfacial structure of water does depend on more than one surface property, as it reflects several factors such as symmetry, lattice parameters and binding energy.

[a] *Physical Chemistry I, Faculty of Chemistry, Bielefeld University, 33615 Bielefeld, Germany. E-mail: fschneider8@uni-bielefeld.de*
[b] *Theoretical Materials Physics, Paderborn University, 33098 Paderborn, Germany*
[c] *Atmospheric and Physical Chemistry, Faculty of Chemistry, Bielefeld University, Bielefeld, 33615, Germany*

A particularly interesting example is calcite, which strongly interacts with water but is known for its surprisingly low ice-nucleating efficacy.[8,29–32] The most stable cleavage plane of calcite, namely calcite (10.4), has been studied intensively. The clean calcite surface undergoes a (2 × 1) reconstruction in ultrahigh vacuum (UHV).[33–36] This reconstruction manifests itself in the rotation of every second carbonate row. The adsorption (and desorption) of water on (and from) calcite has been investigated by temperature-programmed desorption (TPD)[37] and atomic force microscopy (AFM) measurements.[38–40] These studies have revealed that water preferentially adsorbs on top of the unreconstructed carbonate rows. This preference is strong enough to gradually lift the reconstruction at coverages higher than half a monolayer. These UHV investigations of water coverages up to one monolayer have been complemented by several studies at ambient conditions, investigating the hydration layers of bulk water on top of calcite.[41–44]

However, the intermediate regime of water multilayer coverage has rarely been studied, but this regime is essential to understand the low ice-nucleating efficacy of calcite. Here, we combine AFM measurements following the layer-by-layer growth of water layers at low temperatures with TPD measurements to determine the stability of these layers. High-resolution imaging reveals that, although all layers are commensurate to the calcite surface lattice, each water layer adopts a different superstructure. Only after the completion of the fourth layer, ice crystals nucleate and then grow at the expense of the fourth layer, suggesting that the water molecules in the fourth layer are metastable with respect to ice. In contrast, the first three water layers remain intact after ice crystal formation, implying that the water molecules in the first three water layers are more stable than the formed ice crystals. The formed ice crystals are randomly oriented, indicating a poor lattice match with the underlying water layers that are governed by the calcite surface dimensions. Thus, the strong binding of multilayer water to calcite in a structure significantly different from ice provides an explanation for calcite's poor ice-nucleating efficacy.

2. Results and discussion

Previous research of water on calcite at low temperatures has focused on the first water layer, which adopts a (1 × 1) superstructure with two water molecules adsorbed per bulk-truncated unit cell.[40] The adsorption energy of the water molecules in the first layer is about 1 eV,[37,40] which is significantly larger than the binding energy of water molecules within hexagonal ice (~0.6 eV[45,46]). For two reasons, we expect that this first water layer is not involved in ice nucleation. First, the water molecules are arranged in a geometry that deviates from that of ice, and, thus does not provide binding sites for water molecules to arrange in an ice-like manner. Second, the water molecules are bound more strongly to the surface than water molecules in hexagonal ice, which prevents them from rearranging into an ice-like structure.[27]

Nevertheless, this aspect alone is not sufficient to explain calcite's poor ice-nucleating efficacy as nucleation can also be promoted by further water layers.[28] Hence, we performed density-functional theory (DFT) calculations to investigate the adsorption of water molecules on top of the first monolayer. As a starting point, we reproduced the adsorption geometry of the first monolayer from Heggemann *et al.*,[40] which is shown in Fig. 1A. The potential energy surface of a single water molecule adsorbed on top of this first layer is shown in Fig. 1B. It features

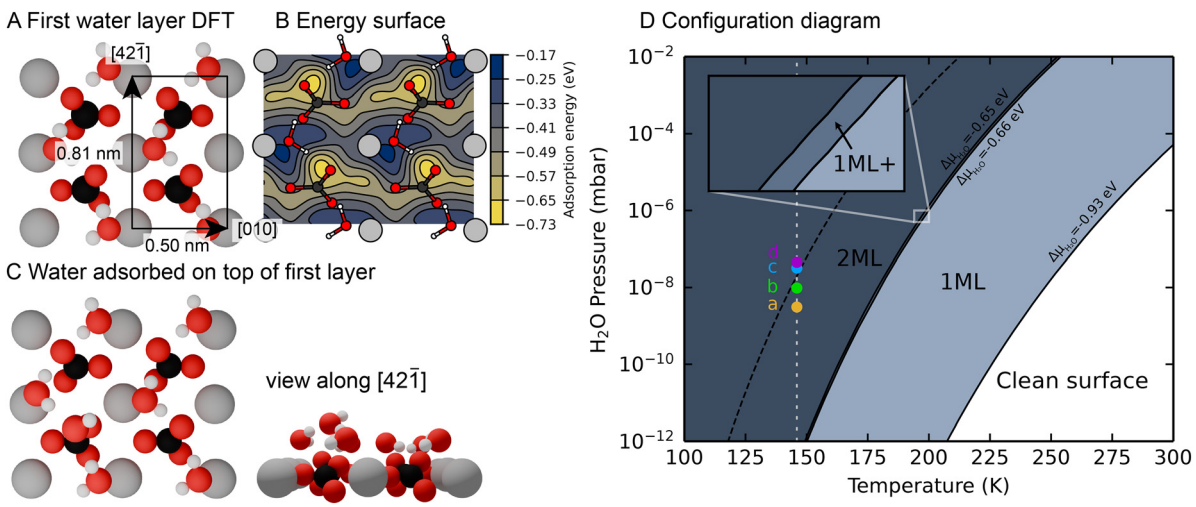

Fig. 1 (A) Adsorption geometry of the first monolayer on calcite calculated by DFT. (B) Potential energy surface of a single water molecule above the first water layer. The displayed molecules constitute the first water layer. (C) Adsorption geometry of a single water molecule on top of the first layer. (D) Calculated (see SI S1 for details) configuration diagram: Solid curves represent water chemical potential values at which phase transitions occur. Each stable phase corresponds to a surface with different water coverage and is labelled accordingly. The inset shows the narrow region where additional water molecules on top of the first layer are stable before the second layer forms. On the vertical dashed line at 146 K the vapor pressure measurements for different water coverages are shown: a second layer (yellow), b third layer (green), c fourth layer (blue), and d ice crystals (purple). We are not able to determine the vapor pressure of the first layer at 146 K as it is below the base pressure of our experimental setup. The dashed black curve is the vapor pressure of ice according to Murphy and Koop.[52]

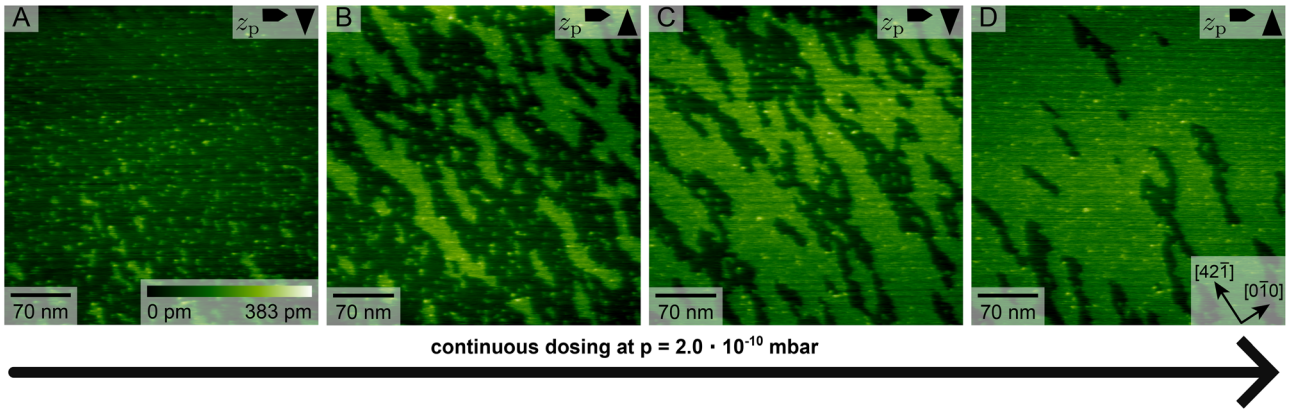

Fig. 2 (A–D) Large-scale AFM images of the growing second layer. Each image corresponds to 350 s of acquisition time. The colour scale in (A) and direction arrows in (D) apply to all images.

two adsorption sites per bulk-truncated unit cell. The corrugation of this potential energy surface is rather small, suggesting a high diffusivity of the water molecules in the second layer. Top and side views of the optimal binding geometry of a single water molecule on top of the first layer are shown in Fig. 1C. Configurations with up to four water layers are observed in the experiment but not calculated here. The energetics of water adsorption (see SI S1 for details) are summarized in the configuration diagram shown in Fig. 1D. In a dry environment at low water pressure and high temperature (*i.e.* low water chemical potential), the bare $CaCO_3$ surface without adsorbed water is the most stable configuration. At higher water pressures and/or lower temperatures, configurations with water molecules adsorbed on the surface are thermodynamically favoured. Calcite with adsorbed water forming one full monolayer (1 ML) is the stable phase above $\Delta\mu_{H_2O} = -0.93$ eV (calculated here with respect to bulk water). This configuration is the most stable one for a wide range of temperatures and water pressures. At a chemical potential of $\Delta\mu_{H_2O} = -0.66$ eV† a second layer configuration with one water molecule per (2×1) unit cell adsorbed on top of the first water layer (see Fig. 1C), is the most stable configuration. Configurations including a full second layer of water are the most stable at chemical potentials above $\Delta\mu_{H_2O} = -0.65$ eV.† Since the vapor pressures of configurations with first- and second-layer water molecules are smaller than the vapor pressure of ice these configurations are thermodynamically more stable than ice.

In a first AFM experiment, we investigated the water structures that form at a sample temperature of 118 K, where water is expected to form amorphous ice upon condensation from the vapor phase. Further, we performed TPD measurements to determine the relative stabilities of the observed water structures. In a second AFM experiment, we repeated the water deposition experiment at a sample temperature of 146 K. In the latter case, the temperature is high enough for crystalline ice to be formed.

2.1 Atomic force microscopy measurements at 118 K

To investigate the growth of the second water layer, we performed AFM measurements at 118 K. At this temperature, the sticking coefficient of water is expected to be close to one, implying that each water molecule colliding with the surface is expected to adsorb and remain on the surface. We adjusted the water pressure in our vacuum chamber to about 2×10^{-10} mbar. By simultaneous AFM measurements, we can to track the growth process of water layers. After filling all adsorption sites on bare calcite with first layer water, further water exposure results in the nucleation of islands shown in Fig. 2A. These islands, which are elongated along the [42$\bar{1}$] direction, gradually grow until they coalesce into a continuous second-layer water film on top of the first water layer (Fig. 2B–D).

Continued water exposure led to the growth of a third and fourth water layer. While the dosage time needed to form the second and third layer is about the same as for the first water layer, filling the fourth water layer takes about twice as long. Assuming a constant sticking coefficient, the second and third layer each contain two water molecules per bulk-truncated unit cell like the first layer, while the fourth layer contains twice as much, *i.e.* four water molecules per unit cell. This finding suggests that the fourth layer indeed consists of two monolayers and, thus, a total coverage of five ML is reached at the end of the layer-by-layer growth regime. Note that the assumption of a constant sticking coefficient is supported by our TPD measurements (see below), revealing no desorption at 140 K, *i.e.*, a sticking coefficient of 1. Moreover, the integral of the respective peaks strongly suggests the fourth layer to be a double layer. Upon further water exposure, the nucleation and growth of ice clusters on top of the fourth layer is observed at 118 K.‡ Due to their undefined morphology and the sample temperature being well below the glass transition temperature of water ($T_g = 136$ K[47–49]), we expect that the formed clusters are amorphous. Exemplary high-resolution images taken on each

† By considering the obtained values, it should be kept in mind that they contain approximations such as the neglect of vibrational entropy and nuclear quantum effects.

‡ We also performed AFM experiments at 146 K, which we will discuss further down. In these experiments we see the same water layers forming. However, instead of amorphous ice crystalline ice is formed.

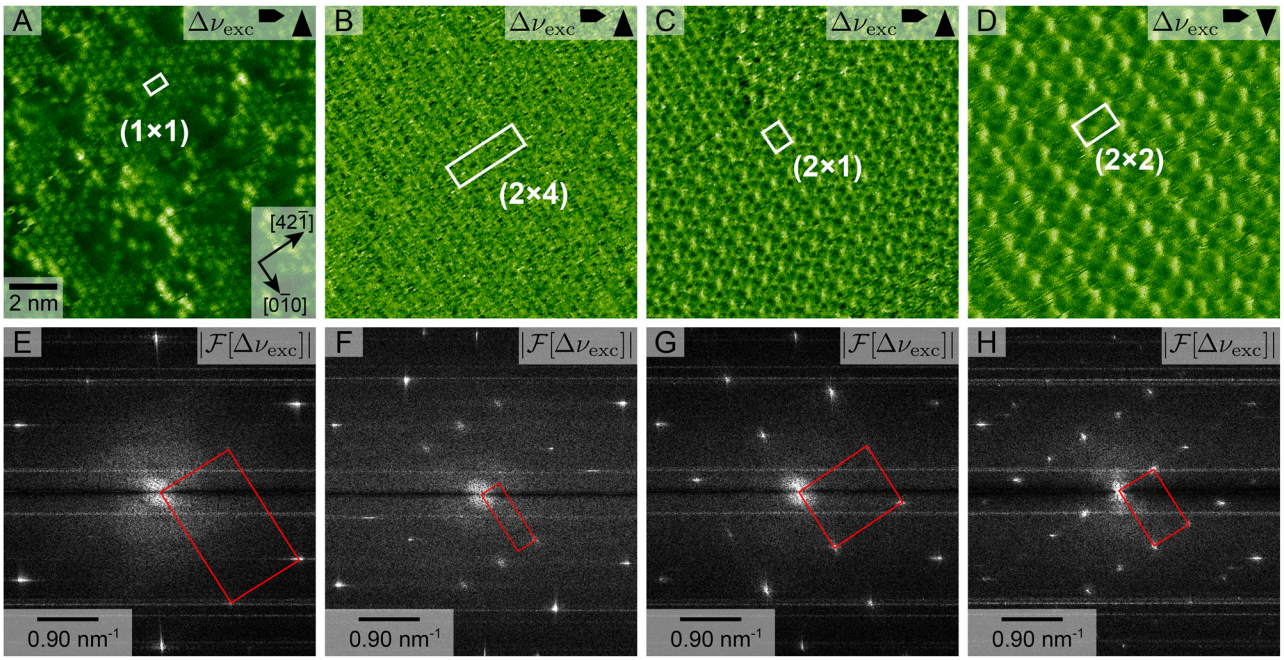

Fig. 3 (A–D) High-resolution AFM images of the first (A), second (B), third (C) and fourth (D) water layer. (E–H) Fourier transformations derived from large-scale AFM images (100 nm × 100 nm) of each water layer. The corresponding large-scale AFM images are shown in SI Fig. S2.

of the grown layers are given in Fig. 3, while the full image series is shown in SI Fig. S1.

In the AFM image in Fig. 3A, the known (1 × 1) structure of the first water layer is shown as a reference. At first glance, the second layer (Fig. 3B) appears less ordered and rather fuzzy. This is in very good agreement with the less corrugated potential energy surface of a single water adsorbed on top of the first layer, as predicted by DFT (Fig. 1B). The corresponding fast Fourier transform (FFT) of the AFM image reveals a (2 × 4) superstructure (Fig. 3F).§ The third layer is again well-ordered with a (2 × 1) superstructure as shown in Fig. 3C and G. Finally, the fourth layer has a (2 × 2) superstructure as shown in Fig. 3D and H. In accordance with its longer growth time, the apparent height of the fourth layer is larger than those of the previous layers as seen in SI Fig. S4.¶ From these results we conclude that in total four water layers grow in a layer-by layer fashion corresponding to five ML, *i.e.*, 10 water molecules per bulk-truncated surface unit cell. All four layers are commensurate to the calcite surface.

2.2 Temperature programmed desorption measurements

To elucidate the relative stability of the water layers, we performed TPD measurements. The measured desorption curves are presented in Fig. 4. In these experiments, we observe the formation of up to six desorption peaks, which we will refer to as α, β, γ, δ, ε and ζ starting with the peaks formed at the smallest initial water coverages.[37] As stated above, the first layer water is bonded much stronger than the second layer water or water in crystalline ice. A higher binding energy corresponds to desorption at a higher temperature. Hence, we assign the observed α,β-double peak at high temperatures, which forms at the lowest initial coverages, to the first water layer.[37] The observed double peak structure is a consequence of the (2 × 1) reconstruction of the bare calcite (10.4) surface, which results in two distinct adsorption positions with different adsorption energies.[37] At water coverages above 0.5 ML, the (2 × 1) reconstruction is gradually lifted.[40] Thus, the (2 × 1) reconstruction is not expected to influence the adsorption of further water layers. At initial coverages above one monolayer, the γ peak is observed at about 165 K, followed by the δ peak at about 164 K. These peaks can be assigned to the second and third layer. In the coverage regime between three and five monolayers, the ε peak is observed. This peak can be assigned to the fourth water layer. At initial coverages beyond five monolayers, the ε peak evolves into a ζ peak. Next, we comment on the shape of the leading edge. Below 156 K, the gradient of the desorption curves with initial coverages above 5 ML matches that with initial coverages between 3 and 5 ML. However, at 156 K, the gradient of the desorption rate decreases, resulting in the formation of a shoulder at about 158 K followed by the ζ peak starting at about 164 K. This finding can be explained by the phase transition from amorphous to crystalline ice, resulting in a crystallization peak/shoulder (*cf.* Fig. 4B and C).[50,51] The existence of this crystallization peak/shoulder strongly supports our previous assignment of the ice clusters grown at 118 K being amorphous. The shift to higher temperatures between

§ The extinction of several spots can be explained by a complicated basis. Further details can be found in SI S2.

¶ We note that the apparent height of the fourth layer is more than twice the height of the second or third layer. However, the apparent height is a result of both the true topographic height and the different force on upper and lower layer. Thus, the apparent height should be interpreted with care and is not sufficient to differentiate single and double layers alone.

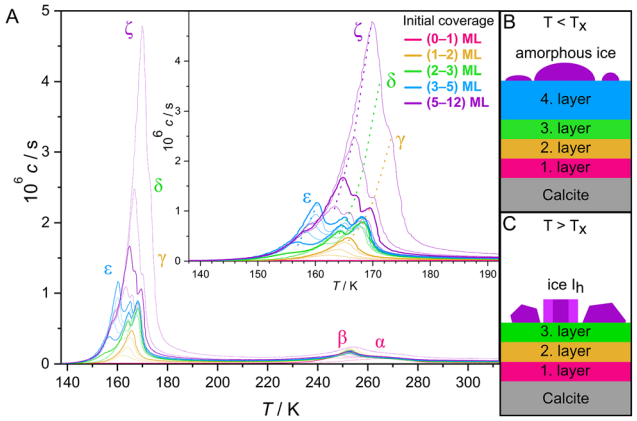

Fig. 4 (A) TPD curves with different initial coverages ranging from 0.4 to 12 ML. The curves corresponding to 1, 2, 3, 4, 5 and 6 ML are depicted as thick lines. The inset shows a zoom into the multilayer temperature window. The dashed lines indicate the peak evolution of the γ to ζ peak. (B) Schematic illustration showing four water layers with amorphous ice clusters on top. This image describes the situation at the beginning of the TPD experiment for high initial coverages (violet curves in A). (C) If the temperature exceeds the crystallization temperature Tx the amorphous ice clusters rearrange to form crystalline ice and the metastable fourth layer vanishes. The shown illustration describes the situation in the TPD experiments at about 158 K for high initial coverages (violet curves in A).

the ε and ζ peak indicates that the water molecules of the fourth water layer are bound less strongly than water molecules in ice. Consequently, the fourth layer is metastable with respect to crystalline ice and, thus, shrinks as soon as crystalline ice forms. Due to the equally shaped leading edge, water in the fourth water layer is approximately as strongly bound as water in amorphous ice.

2.3 Atomic force microscopy measurements at 146 K

To investigate how crystalline ice forms on the calcite (10.4) surface, we performed AFM measurements at a sample temperature of about 146 K. This temperature is above the glass transition temperature T_g = 136 K of water.[47–49] Hence, instead of amorphous ice, crystalline ice should nucleate when the water partial pressure is sufficiently high. At 146 K, hexagonal ice becomes thermodynamically stable at vapor pressures above $p = 2.01 \times 10^{-8}$ mbar.[52] However, due to the kinetic barrier of the nucleation process, higher pressures are required to initiate ice nucleation. We gradually increased the water partial pressure to determine the pressure needed for the formation of each water layer and of crystalline ice. In these experiments we used the aforementioned distinct superstructures of each layer as finger print to unambiguously identify which layer has formed. The second water layer is observed to form above $p \approx 3.1 \times 10^{-9}$ mbar, the third water layer above $p \approx 9.7 \times 10^{-9}$ mbar and the fourth water layer above $p \approx 3.2 \times 10^{-8}$ mbar (see SI Fig. S5). These partial pressures are indicated in the configuration diagram (Fig. 1D). The pressure needed to form the second layer is well below the equilibrium vapor pressure of hexagonal ice, in line with the TPD experiments demonstrating that water in this layer is stronger bound than in ice. The third layer forms at a pressure close to the equilibrium vapor pressure of hexagonal ice. Based on this finding, the stability of the third layer is comparable to that of crystalline ice. The δ peak (corresponding to desorption of the third layer) in our TPD data is situated at slightly higher temperature compared to the ζ peak (corresponding to desorption of crystalline ice). This finding indicates that the third layer is more stable as compared to ice. Alternatively, the third layer might be a kinetically trapped configuration which is slightly less stable than crystalline ice. The pressure needed to form the fourth layer is above the equilibrium vapor pressure of hexagonal ice, just as expected from its lower stability as compared to ice. We observed ice crystal formation at pressures above $p \approx 4.5 \times 10^{-8}$ mbar.‖ Freshly nucleated ice clusters are shown in Fig. 5A.[53]** Oval shaped depressions around these ice clusters are seen in the AFM images, which are holes in the fourth layer. These holes are observed to grow in time which we interpret as consumption of the fourth water layer by the ice crystals. High-resolution images of the area around the clusters are shown in Fig. 5B. They reveal the remaining water layer exhibits a (2 × 1) superstructure, which is the finger print of the third water layer (*cf.* Fig. 3).

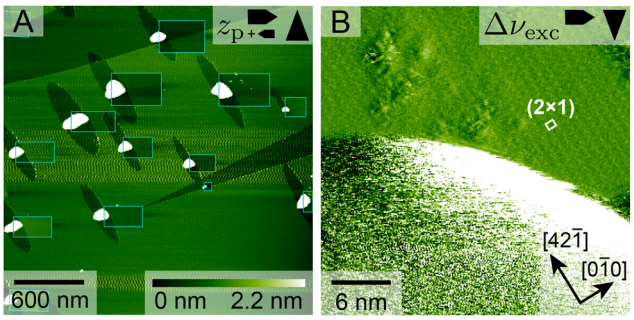

Fig. 5 (A) Large-scale AFM image of the beginning of cluster growth. Oval holes (dark) inside the fourth water layer are seen around each cluster (white). To reveal the true cluster shape, trace and retrace (image parts marked by a blue rectangle) images are combined, following a strategy as presented in ref. 53. (B) High-resolution AFM image of a cluster (bright, lower half) and the surrounding water layer with the (2 × 1) unit cell indicated by a white rectangle.

‖ The pressures reported here match perfectly with what is expected from thermodynamic numbers. We want to note, however, that both our temperature and pressure measurements might have errors as we are not able to measure these properties directly at the surface of our sample. The good match between observed and expected pressure based on the vapor pressure of hexagonal ice indicates that these errors are small and/or temperature and pressure measurement errors cancel each other as a higher surface temperature results in a higher vapor pressure of hexagonal ice.

** We want to emphasize that we had to find a compromise between the optimal feedback-loop parameters to image flat surface areas with holes of a depth of a few hundred picometres and the parameters to image clusters with heights of up to 25 nm at the same time. This results in two image artifacts: firstly, the cluster shape is elongated in the fast-scanning direction as the feedback-loop is too slow to approach the flat surface at the end of the cluster fast enough (*cf.* SI Fig. S6, showing trace and retrace). However, the true cluster shape can be revealed by combining trace and retrace images in analogy to the strategy introduced by Martin-Jimenez *et al.*:[53] the right part of each cluster, which is correctly imaged by the retrace image is shown as an overlay on top of the trace image, which correctly images the left part of each cluster. Secondly, artificial vibrations are present in flat surface areas (in particular in the center of the image).

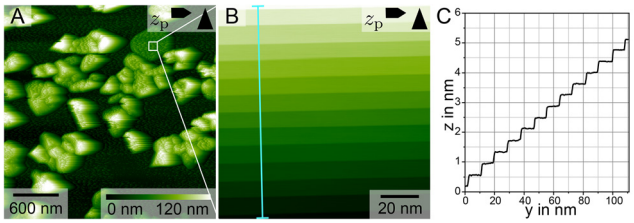

Fig. 6 (A) Large-scale AFM images of ice crystals after 50 min of growth at $p \approx 8.3 \times 10^{-8}$ mbar. An ice crystal with its basal plane parallel to the calcite surface is marked by a white square. (B) Zoom onto the marked cluster. Each step corresponds to the epitaxial growth of a crystalline ice layer. (C) Height profile along the light blue line shown in (B). The height of each step is (0.392 ± 0.029) nm.

Consequently, the first three layers are observed to remain stable upon cluster formation, while the fourth layer shrinks implying that ice clusters are thermodynamically favored over the fourth layer while the first three layers are more stable as compared to the clusters. These findings suggest that the formed ice clusters are crystalline. Fig. 6A shows ice crystals after 50 min of growth at $p \approx 8.3 \times 10^{-8}$ mbar. Ice nucleates somewhat randomly oriented at the high saturation ratio of $S = 4.1$ in our experiment. One of the observed ice crystals (marked by a white square in Fig. 6A) grows with its basal plane parallel to the calcite surface. AFM measurements on top of this particular crystal revealed layer-by-layer growth of hexagonal ice. Under these conditions ice grows fast as compared to our AFM scan speed. Hence, the layer-by-layer growth is depicted in an AFM image by equally separated, ascending steps along the fast-scan direction, as can be seen in Fig. 6B." The height profile along this direction is shown in Fig. 6C. The observed step height is (0.392 ± 0.029) nm, which corresponds nicely to the length of half an elementary cell along the *c*-axis of hexagonal ice and, thus, agrees with the separation between two buckled bilayers.[54] This finding, thus, provides strong evidence for the fact that the formed clusters are indeed crystalline hexagonal ice.

The observed ice crystals exhibit a large variety of orientations. This finding implies that the calcite surface does not promote the nucleation of any particular facet of ice. Instead, the water layer structure forming on calcite appears to provide a hydrophobic surface for crystalline ice. The reason for this hydrophobicity might be a combination of the non-ice-like interfacial water structure which is templated by the calcite surface and the strong binding of water within these layers towards the calcite surface which prevents them from rearranging into an ice-like structure.

3. Conclusions

In this study, we investigated the nucleation and growth of water multilayers and ice on the calcite (10.4) surface. We observed the growth of four well-ordered water layers with distinct superstructures, followed by the nucleation of either amorphous or crystalline ice depending on the sample temperature. Each layer exhibits a superstructure commensurate to the calcite lattice. Furthermore, up to three water layers are thermodynamically more stable than crystalline ice, while the fourth layer is metastable with respect to crystalline ice and shrinks as soon as crystalline ice forms. The nucleated ice crystals are randomly oriented, underlining the poor ice nucleation efficacy of calcite. The strong binding and consequently low structural flexibility of the first three water layers on calcite, together with their non-ice-like structure, provide an explanation for calcite's poor ice-nucleating efficacy.

4. Methods

4.1 Experimental methods

All experiments were performed under UHV conditions with a base pressure well below 10^{-10} mbar. The calcite crystals (Korth Kristalle, Germany) were mounted into a homebuilt sample holder.[55] The temperature was measured using a Type K thermocouple located as close as possible to the sample surface. The orientation of each calcite crystal within the sample holder was determined using the crystal's birefringence. The transfer into the UHV system included degassing the samples at 400 K overnight. In the UHV system, the crystals were degassed at 750 K for 60 min and then cleaved *in situ* with a scalpel blade. To reduce surface charges, the cleaved crystals were annealed at 500 K for 60 min before AFM measurements started. The liquid water source was degassed through several freeze–pump–thaw cycles, and then the water was introduced into the chamber *via* a leak valve directed towards the sample inside the AFM.

AFM experiments. The AFM measurements were done in frequency-modulation mode using an Omicron AFM VT XA (Omicron, Germany) and cantilevers of type PPP-NCH (Nanosensors, Switzerland). The cantilevers were glued onto a commercial tip holder (Omicron, Germany) and degassed in the load lock at 400 K overnight. The cantilevers were sputtered with Ar^+ ions (2000 eV). The sample was cooled inside the AFM with liquid nitrogen to either (118 ± 1) K or (146 ± 1) K and kept at this temperature (measured on the sample holder) during measurements. We note that due to calcite's low thermal conductivity, the sample temperature may differ. To compensate for linear thermal drift, we corrected the AFM images using unDrift.[56]

TPD experiments. The TPD measurements were done on a liquid-nitrogen cooled manipulator with a resistive heater. The sample holder was cooled to about 120 K before each measurement. At the start of each measurement session, we performed a clean TPD measurement without prior dosing of any water. During the TPD experiments, the sample temperature was increased linearly at a heating rate of $\beta = 1$ K s^{-1} The desorbing molecules were detected using a quadrupole mass spectrometer (Hiden, U.K.) mounted inside a glass shroud. With its aperture, it is positioned closer than 1 mm to the sample surface during the measurement to minimize detection of molecules desorbing from other surfaces.

4.2 Theoretical methods

DFT calculations are performed using the Vienna *ab initio* simulation package (VASP).[57] The electron–ion interactions

are described in the projector-augmented wave (PAW)[58,59] scheme.

The electronic exchange and correlation interactions are treated in the General Gradient Approximation (GGA) with the PBE[60] functional. The validity of the PBE functional has been verified in previous studies as this functional has been shown to constitute a good descriptor for both the calcite surface[34] and water.[61,62] The wave functions are expanded in plane waves up to an energy cutoff of 520 eV, 30% larger than the recommended value for oxygen to assure convergence.

London dispersion corrections are included through Grimme's DFT-D3 approximation[63] with the Becke–Johnson damping function.[64] The calcite (10.4) semi-infinite surface is modelled by a (2×1) slab of roughly 20 Å thickness consisting of 7 layers adding to a total number of 144 atoms. The slab is modelled within an orthorhombic cell with dimension $10.07 \times 8.11 \times 40.00$ Å^3 leaving approximately 20 Å of vacuum in the normal direction to the surface. A dipole correction is used to minimize spurious interactions across the vacuum originating from the periodic boundary conditions and the non-equivalent slab surfaces. The surface Brillouin zone is sampled with a Γ-centered $3 \times 3 \times 1$ k-point mesh. all structures are relaxed until the forces acting on the ions are lower than 0.002 eV Å^{-1}.

Author contributions

FS performed the AFM experiments. LK carried out the TPD experiments. FS and LK analyzed the experimental data with contributions of RB, TK and AK. The DFT calculations were done by IARA and WGS. The first version of the manuscript was written by FS. All authors commented on and contributed to the final manuscript.

Conflicts of interest

There are no conflicts to declare.

Data availability

Data used in the study are included in the manuscript and/or supplementary information (SI). Supplementary information: further details regarding the DFT calculations to determine the configuration diagram, structure of the second layer and further AFM images. See DOI: https://doi.org/10.1039/d6cp01936f.

Acknowledgements

We gratefully acknowledge support from the Deutsche Forschungsgemeinschaft (DFG) through projects KU1980/15-1 and SCHM1361/35-1.

Notes and references

1 H. Cölfen, Biomineralization: A crystal-clear view, *Nat. Mater.*, 2010, **9**, 960–961.
2 T. Yamazaki, Y. Kimura, P. G. Vekilov, E. Furukawa, M. Shirai, H. Matsumoto, A. E. S. van Driessche and K. Tsukamoto, Two types of amorphous protein particles facilitate crystal nucleation, *Proc. Natl. Acad. Sci. U.S.A.*, 2017, **114**, 2154–2159.
3 T. Koop, B. Luo, A. Tsias and T. Peter, Water activity as the determinant for homogeneous ice nucleation in aqueous solutions, *Nature*, 2000, **406**, 611–614.
4 B. J. Murray, S. L. Broadley, T. W. Wilson, S. J. Bull, R. H. Wills, H. K. Christenson and E. J. Murray, Kinetics of the homogeneous freezing of water, *Phys. Chem. Chem. Phys.*, 2010, **12**, 10380–10387.
5 G. Renzer, I. de Almeida Ribeiro, H.-B. Guo, J. Fröhlich-Nowoisky, R. J. Berry, M. Bonn, V. Molinero and K. Meister, Hierarchical assembly and environmental enhancement of bacterial ice nucleators, *Proc. Natl. Acad. Sci. U.S.A.*, 2024, **121**, e2409283121.
6 C. Hoose and O. Möhler, Heterogeneous ice nucleation on atmospheric aerosols: a review of results from laboratory experiments, *Atmos. Chem. Phys.*, 2012, **12**, 9817–9854.
7 B. J. Murray, D. O'Sullivan, J. D. Atkinson and M. E. Webb, Ice nucleation by particles immersed in supercooled cloud droplets, *Chem. Soc. Rev.*, 2012, **41**, 6519–6554.
8 J. D. Atkinson, B. J. Murray, M. T. Woodhouse, T. F. Whale, K. J. Baustian, K. S. Carslaw, S. Dobbie, D. O'Sullivan and T. L. Malkin, The importance of feldspar for ice nucleation by mineral dust in mixed-phase clouds, *Nature*, 2013, **498**, 355–358.
9 T. Koop and B. Zobrist, Parameterizations for ice nucleation in biological and atmospheric systems, *Phys. Chem. Chem. Phys.*, 2009, **11**, 10839–10850.
10 M. A. Holden, J. M. Campbell, F. C. Meldrum, B. J. Murray and H. K. Christenson, Active sites for ice nucleation differ depending on nucleation mode, , 2021, **118**, e2022859118.
11 R. W. Friddle and K. Thürmer, How nanoscale surface steps promote ice growth on feldspar: microscopy observation of morphology-enhanced condensation and freezing, *Nanoscale*, 2019, **11**, 21147–21154.
12 M. A. Holden, T. F. Whale, M. D. Tarn, D. O'Sullivan, R. D. Walshaw, B. J. Murray, F. C. Meldrum and H. K. Christenson, High-speed imaging of ice nucleation in water proves the existence of active sites, *Sci. Adv.*, 2019, **5**, eaav4316.
13 A. Kiselev, F. Bachmann, P. Pedevilla, S. J. Cox, A. Michaelides, D. Gerthsen and T. Leisner, Active sites in heterogeneous ice nucleation-the example of K-rich feldspars, *Science*, 2017, **355**, 367–371.
14 R. O. David, C. Marcolli, J. Fahrni, Y. Qiu, Y. A. Perez Sirkin, V. Molinero, F. Mahrt, D. Brühwiler, U. Lohmann and Z. A. Kanji, Pore condensation and freezing is responsible for ice formation below water saturation for porous particles, *Proc. Natl. Acad. Sci. U.S.A.*, 2019, **116**, 8184–8189.
15 P. Yan, Y. Hou, H. Zheng and M. Liu, Ultrafast laser-assisted hybrid fabrication of biomimetic superhydrophobic surfaces: strategies, mechanisms, and applications, *Nanoscale*, 2025, **17**, 21400–21422.

16 P. Eberle, M. K. Tiwari, T. Maitra and D. Poulikakos, Rational nanostructuring of surfaces for extraordinary icephobicity, *Nanoscale*, 2014, **6**, 4874–4881.
17 S. Bahal, J. Zhang, V. Singh, P. Kabi, A. Heydari and M. K. Tiwari, Tunable icephobicity of surface-grown metal-organic frameworks with nanohierarchical texture, *Nanoscale*, 2026, **18**, 7485–7500.
18 S. A. Alsalhi, J. Bath, A. Turberfield and W. Schwarzacher, Ice nucleation by DNA origami, *Nanoscale*, 2025, **17**, 16616–16621.
19 M. Henderson, The interaction of water with solid surfaces: fundamental aspects revisited, *Surf. Sci. Rep.*, 2002, **46**, 1–308.
20 T. K. Shimizu, S. Maier, A. Verdaguer, J.-J. Velasco-Velez and M. Salmeron, Water at surfaces and interfaces: From molecules to ice and bulk liquid, *Prog. Surf. Sci.*, 2018, **93**, 87–107.
21 P. A. Thiel and T. E. Madey, The interaction of water with solid surfaces: Fundamental aspects, *Surf. Sci. Rep.*, 1987, **7**, 211–385.
22 A. Michaelides, V. A. Ranea, P. L. de Andres and D. A. King, General model for water monomer adsorption on close-packed transition and noble metal surfaces, *Phys. Rev. Lett.*, 2003, **90**, 216102.
23 A. Hodgson and S. Haq, Water adsorption and the wetting of metal surfaces, *Surf. Sci. Rep.*, 2009, **64**, 381–451.
24 C. Valeriani, Deep learning for unravelling features of heterogeneous ice nucleation, *Proc. Natl. Acad. Sci. U.S.A.*, 2022, **119**, e2211295119.
25 M. B. Davies, M. Fitzner and A. Michaelides, Accurate prediction of ice nucleation from room temperature water, *Proc. Natl. Acad. Sci. U.S.A.*, 2022, **119**, e2205347119.
26 M. Fitzner, P. Pedevilla and A. Michaelides, Predicting heterogeneous ice nucleation with a data-driven approach, *Nat. Commun.*, 2020, **11**, 4777.
27 P. Pedevilla, M. Fitzner and A. Michaelides, What makes a good descriptor for heterogeneous ice nucleation on OH-patterned surfaces, *Phys. Rev. B*, 2017, **96**, 115441.
28 M. Fitzner, G. C. Sosso, S. J. Cox and A. Michaelides, The Many Faces of Heterogeneous Ice Nucleation: Interplay Between Surface Morphology and Hydrophobicity, *J. Am. Chem. Soc.*, 2015, **137**, 13658–13669.
29 J. D. Yakobi-Hancock, L. A. Ladino and J. P. D. Abbatt, Feldspar minerals as efficient deposition ice nuclei, *Atmos. Chem. Phys.*, 2013, **13**, 11175–11185.
30 F. Zimmermann, S. Weinbruch, L. Schütz, H. Hofmann, M. Ebert, K. Kandler and A. Worringen, Ice nucleation properties of the most abundant mineral dust phases, *J. Geophys. Res.: Atmos.*, 2008, **113**, D23204.
31 M. L. Eastwood, S. Cremel, C. Gehrke, E. Girard and A. K. Bertram, Ice nucleation on mineral dust particles: Onset conditions, nucleation rates and contact angles, *J. Geophys. Res.: Atmos.*, 2008, **113**, D22203.
32 T. Zolles, J. Burkart, T. Häusler, B. Pummer, R. Hitzenberger and H. Grothe, Identification of ice nucleation active sites on feldspar dust particles, *J. Phys. Chem. A*, 2015, **119**, 2692–2700.
33 R. Demichelis, P. Raiteri and J. D. Gale, Reconstruction of the {10$\bar{1}$4} Calcite Surface: When, How, and Why, *J. Phys. Chem. C*, 2025, **129**, 22555–22560.
34 J. Heggemann, Y. S. Ranawat, O. Krejčí, A. S. Foster and P. Rahe, Differences in Molecular Adsorption Emanating from the (2 × 1) Reconstruction of Calcite(104), *J. Phys. Chem. Lett.*, 2023, **14**, 1983–1989.
35 J. Schütte, P. Rahe, L. Tröger, S. Rode, R. Bechstein, M. Reichling and A. Kühnle, Clear signature of the (2 x 1) reconstruction of calcite (1014), *Langmuir*, 2010, **26**, 8295–8300.
36 S. Stipp, Toward a conceptual model of the calcite surface: hydration, hydrolysis, and surface potential, *Geochim. Cosmochim. Acta*, 1999, **63**, 3121–3131.
37 T. Dickbreder, D. Lautner, A. Köhler, L. Klausfering, R. Bechstein and A. Kühnle, How water desorbs from calcite, *Phys. Chem. Chem. Phys.*, 2023, **25**, 12694–12701.
38 L. Klausfering, F. Schneider, R. Bechstein and A. Kühnle, Reconstruction of calcite (10.4) manifests itself in the tip-assisted diffusion of water, , 2025, **751**, 122598.
39 J. Heggemann, J. Huang, S. Aeschlimann, S. Spiller, A. S. Foster and P. Rahe, Sidestepping Intermolecular Hydrogen Bonds: How Single Water Molecules Adsorb and Assemble on the Calcite(104)-(2 × 1) Surface, *ACS Nano*, 2025, **19**, 26650–26658.
40 J. Heggemann, S. Aeschlimann, T. Dickbreder, Y. S. Ranawat, R. Bechstein, A. Kühnle, A. S. Foster and P. Rahe, Water adsorption lifts the (2 × 1) reconstruction of calcite(104), *Phys. Chem. Chem. Phys.*, 2024, **26**, 21365–21369.
41 H. Imada, K. Kimura and H. Onishi, Water and 2-propanol structured on calcite (104) probed by frequency-modulation atomic force microscopy, *Langmuir*, 2013, **29**, 10744–10751.
42 F. Heberling, T. P. Trainor, J. Lützenkirchen, P. Eng, M. A. Denecke and D. Bosbach, Structure and reactivity of the calcite-water interface, *J. Colloid Interface Sci.*, 2011, **354**, 843–857.
43 H. Söngen, S. J. Schlegel, Y. Morais Jaques, J. Tracey, S. Hosseinpour, D. Hwang, R. Bechstein, M. Bonn, A. S. Foster, A. Kühnle and E. H. G. Backus, Water Orientation at the Calcite-Water Interface, *J. Phys. Chem. Lett.*, 2021, **12**, 7605–7611.
44 P. Geissbühler, P. Fenter, E. DiMasi, G. Srajer, L. B. Sorensen and N. C. Sturchio, Three-dimensional structure of the calcite–water interface by surface X-ray scattering, *Surf. Sci.*, 2004, **573**, 191–203.
45 B. Santra, J. Klimeš, D. Alfè, A. Tkatchenko, B. Slater, A. Michaelides, R. Car and M. Scheffler, Hydrogen bonds and van der Waals forces in ice at ambient and high pressures, *Phys. Rev. Lett.*, 2011, **107**, 185701.
46 E. Whalley, Energies of the phases of ice at zero temperature and pressure, *J. Chem. Phys.*, 1984, **81**, 4087–4092.
47 A. Hallbrucker, E. Mayer and G. P. Johari, Glass-liquid transition and the enthalpy of devitrification of annealed vapor-deposited amorphous solid water: a comparison with hyperquenched glassy water, *J. Phys. Chem.*, 1989, **93**, 4986–4990.

48 A. Hallbrucker, E. Mayer and G. P. Johari, The heat capacity and glass transition of hyperquenched glassy water, *Philos. Mag. B*, 1989, **60**, 179–187.
49 G. A. Kimmel, M. K. Dunlap, K. Gurdumov, R. S. Smith, L. Kringle and B. D. Kay, Translational diffusion in supercooled water at and near the glass transition temperature-136 K, *J. Chem. Phys.*, 2025, **162**, 244505.
50 R. J. Speedy, P. G. Debenedetti, R. S. Smith, C. Huang and B. D. Kay, The evaporation rate, free energy, and entropy of amorphous water at 150 K, *J. Chem. Phys.*, 1996, **105**, 240–244.
51 R. S. Smith, J. Matthiesen, J. Knox and B. D. Kay, Crystallization kinetics and excess free energy of H2O and D2O nanoscale films of amorphous solid water, *J. Phys. Chem. A*, 2011, **115**, 5908–5917.
52 D. M. Murphy and T. Koop, Review of the vapour pressures of ice and supercooled water for atmospheric applications, *Q. J. R. Meteorolog. Soc.*, 2005, **131**, 1539–1565.
53 D. Martin-Jimenez, Q. Zhong, A. Schirmeisen and D. Ebeling, Imaging the adsorption sites of organic molecules on metallic surfaces by an adaptive tunnelling current feedback, *Nanotechnology*, 2024, **35**, 475703.
54 W. F. Kuhs and M. S. Lehmann, in *Water Science Reviews 2*, ed. F. Franks, Cambridge University Press, 1986, pp. 1–66.
55 L. Tröger, J. Schütte, F. Ostendorf, A. Kühnle and M. Reichling, Concept for support and cleavage of brittle crystals, *Rev. Sci. Instrum.*, 2009, **80**, 63703.
56 T. Dickbreder, F. Sabath, L. Höltkemeier, R. Bechstein and A. Kühnle, unDrift: A versatile software for fast offline SPM image drift correction, *Beilstein J. Nanotechnol.*, 2023, **14**, 1225–1237.
57 G. Kresse and J. Furthmüller, Efficiency of ab-initio total energy calculations for metals and semiconductors using a plane-wave basis set, *Comput. Mater. Sci.*, 1996, **6**, 15–50.
58 P. E. Blöchl, Projector augmented-wave method, *Phys. Rev. B*, 1994, **50**, 17953–17979.
59 G. Kresse and D. Joubert, From ultrasoft pseudopotentials to the projector augmented-wave method, *Phys. Rev. B*, 1999, **59**, 1758–1775.
60 J. P. Perdew, K. Burke and M. Ernzerhof, Generalized Gradient Approximation Made Simple, *Phys. Rev. Lett.*, 1996, **77**, 3865–3868.
61 T. Ohto, M. Dodia, J. Xu, S. Imoto, F. Tang, F. Zysk, T. D. Kühne, Y. Shigeta, M. Bonn, X. Wu and Y. Nagata, Accessing the Accuracy of Density Functional Theory through Structure and Dynamics of the Water-Air Interface, *J. Phys. Chem. Lett.*, 2019, **10**, 4914–4919.
62 M. J. Gillan, D. Alfè and A. Michaelides, Perspective: How good is DFT for water?, *J. Chem. Phys.*, 2016, **144**, 130901.
63 S. Grimme, J. Antony, S. Ehrlich and H. Krieg, A consistent and accurate ab initio parametrization of density functional dispersion correction (DFT-D) for the 94 elements H-Pu, *J. Chem. Phys.*, 2010, **132**, 154104.
64 S. Grimme, S. Ehrlich and L. Goerigk, Effect of the damping function in dispersion corrected density functional theory, *J. Comput. Chem.*, 2011, **32**, 1456–1465.

